Precision Engineering 96 (2025) 729–744

Contents lists available at ScienceDirect

Precision Engineering

journal homepage: www.elsevier.com/locate/precision

Vacuum compatible spring wire system for mass measurement of vials during lyophilization

Steven J. Burcat [a,1], Rohan P. Kadambi [b,1], Lorenzo Stratta [c], Richard D. Braatz [b], Roberto Pisano [c], Bernhardt L. Trout [b], Alexander H. Slocum [a,*]

[a] Department of Mechanical Engineering, Massachusetts Institute of Technology, 77 Massachusetts Ave, Cambridge, 02139, MA, USA
[b] Department of Chemical Engineering, Massachusetts Institute of Technology, 77 Massachusetts Ave, Cambridge, 02139, MA, USA
[c] Department of Applied Science and Technology, Politecnico di Torino, 24 corso Duca degli Abruzzi, Torino, 10129, Italy

ARTICLE INFO

Keywords:
In-situ mass measurement
Helical spring
In-line calibration
Lyophilization

ABSTRACT

Pharmaceutical lyophilization (vacuum freeze-drying) stabilizes aqueous formulations, commonly in vials, by removing 99.9% of their water. Failure to remove enough water leads to unstable products, so measuring the amount of water removed throughout the process is critical. Current technologies can measure the total rate of water removal from a batch of vials or destructively measure the final water content of sample vials, but they cannot monitor individual vials in situ. An in-line measurement for the water content of every vial would assess variation in the drying process, enabling process improvements and vial-specific optimizations. This work presents a mass sensor that achieves this individual vial measurement throughout the lyophilization process.

This mass sensor consists of two partial helical springs holding a suspended vial. As water sublimates from the vial during drying, the position and orientation of the free ends of the helical springs change. This change is amplified by sensing arms and measured by a camera outside of the vacuum chamber. Optical fiducials at the ends of the sensing arms enable high-fidelity measurement of the amplified motion. This sensor provides individual vial mass information, allowing tracking of its sublimation rate, without affecting the lyophilization process.

The sensor design was evaluated by building ten sensors for 10R vials with a 3 mL fill. After calibration, these sensors achieved a median offline testing error of 13 mg, which improved to 6.5 mg when calibration coefficients were updated using the maximum a posteriori method. When the sensors were tested in a lyophilization environment, the median error in their final mass measured increased to 50 mg, likely due to micro-slip of the sensor assembly contact regions between measurements introduced hysteresis. Nevertheless, per vial sublimation rates are measured accurately and used to infer drying endpoints.

1. Introduction

Lyophilization (vacuum freeze-drying) is used in pharmaceutical manufacturing to remove water at cryogenic temperatures by sublimating ice through a porous product cake, protecting temperature-sensitive pharmaceutical products. This removal of water greatly improves the stability of pharmaceutical products, extending their shelf-life and reducing storage condition requirements [1]. In typical pharmaceutical lyophilization, vials are frozen within a chamber, then dried in a two-phase process at pressures below 30 Pa. During the first phase, known as primary drying, heat is carefully supplied to the vials to sublimate the ice. The sublimation rate is limited by collapse phenomena that can occur if the product exceeds a critical temperature, typically between −35 °C and −15 °C during the drying process [2,3]. After the ice has fully sublimed, the second phase, known as secondary drying, occurs, where more heat is applied to facilitate the desorption of the remaining water. While heat is traditionally supplied through a temperature-controlled shelf on which the vials sit, it can also be supplied through radiation [4,5]. The rate limitations during primary drying result in slow pharmaceutical lyophilization cycles, ranging from 10 hr to 1 week. To meet industrial throughput levels, production batches typically range from 1000 to 10,000 vials, which have inherent

* Corresponding author.
E-mail addresses: sburcat@mit.edu (S.J. Burcat), kadambi@mit.edu (R.P. Kadambi), lorenzo.stratta@polito.it (L. Stratta), braatz@mit.edu (R.D. Braatz), roberto.pisano@polito.it (R. Pisano), trout@mit.edu (B.L. Trout), slocum@mit.edu (A.H. Slocum).
[1] Co-first authors.

https://doi.org/10.1016/j.precisioneng.2025.07.007
Received 18 February 2025; Received in revised form 26 June 2025; Accepted 3 July 2025
Available online 25 July 2025

heterogeneity [6]. These large batch sizes and slow dynamics necessitate the accurate detection of individual vial states during both primary and secondary drying to optimize the lyophilization process.

Classical methods for monitoring primary drying in this field include the pressure ratio test, which measures the fraction of water vapor in the head space, and the pressure rise test, which estimates the current total water flux out of the lyophilizer [7–9]. Recent advances, such as the tunable laser diode, absorption spectroscopy (TLDAS) systems, have improved the accuracy of the pressure rise test by enabling continuous monitoring of the water flux [10]. Many studies use both classical and modern versions of these system-level analytics in attempts to optimize the lyophilization process for a large batch of vials [11,12]. Two types of massing systems have been proposed for monitoring the primary drying of single or small groups of vials [13]. However, these systems may not represent the entire batch because the balance changes the amount of radiation experienced by nearby vials [14] and requires specific vial geometries that may not match the production vials [15]. Furthermore, these systems are incompatible with vial handling during automatic loading and unloading operations or continuous lyophilization processes.

Evaluation of secondary drying requires measurement of a final residual water content, typically 0.5 to 4 wt% of the final dry product mass, which is too small to reliably infer from a direct comparison of the initial and final vial masses [16]. Typically, the residual moisture of a subset of the vials in a batch is measured after lyophilization using destructive methods such as Karl Fischer titration or thermogravimetric analysis [1]. Methods based on NIR spectroscopy have been proposed to monitor secondary drying inline [17], but these methods would likely be limited to measuring a few vials at the outer edges of a lyophilization chamber, which are known to have a lower residual water content relative to most of the batch.

System-level analytics, such as the pressure ratio test, pressure rise test, and TLDAS, are inherently limited by their inability to detect failed vials or variation in vial drying rates. Directly measuring the mass change of each vial in the lyophilizer enables this detection, while maintaining full system observability by combining the individual data. Existing vial-specific analytic methods are large, require custom solutions to function in a vacuum, and adapt poorly to larger scales. Additionally, while batch lyophilization has dominated the field for decades, new studies have proposed continuous lyophilization processes that could even more efficiently use per vial mass data by optimizing the conditions each vial experiences and releasing subsets of vials as they finish drying [4,18].

Thus, there exists a need to design a sensor that can tolerate the conditions of lyophilization, maintain a small footprint within the system, and accurately measure the mass of individual vials. This work presents the design and testing of one such sensor for radiative drying applications that uses helical spring wires that deflect based on the changing vial mass during sublimation to track individual vial drying rates.

2. System requirements

An effective single vial mass sensor for lyophilization must resolve both large, $\mathcal{O}(1\ \mathrm{g})$, changes in mass during primary drying and small, $\mathcal{O}(1\ \mathrm{mg})$, changes in mass during secondary drying. This sensor has six functional requirements:

1. The sensor system must operate in a vacuum environment.
2. The sensor must provide individual vial data.
3. The sensor must resolve the final mass of water in a lyophilized cake. The specific mass value varies according to the specific application, as described in Section 2.1, and is typically $\mathcal{O}(1\ \mathrm{mg})$.
4. The sensor must operate in temperature environments as low as −40 °C.
5. The sensing system must accommodate moving vials through a lyophilizer.
6. The sensor design process must be vial-agnostic to enable use with a variety of potential formulations and ease integration with pharmaceutical production.
7. The sensor must be nondestructive.
8. The sensor cannot contaminate the products.

A viable solution, shown in Fig. 1, was achieved by suspending a vial from compliant wires such that an external camera could view optical fiducials attached to the wires to measure wire deflection and hence vial mass. Each sensor holds a single vial and can be viewed through a window by a camera outside a vacuum chamber. This sensor topology does not interfere with the lyophilization process and does not introduce potential contamination sources to the system.

2.1. Sensitivity requirements

This sensor design was tested with 10R vials filled with 3 mL of 95 wt% water solution. A design spreadsheet based on the general method is provided in the supplemental materials, which can be used to determine the appropriate sensor parameters for other applications.

10R vials have an average mass of $m_{\mathrm{vial}} = 9\ \mathrm{g}$ and are typically capped with $m_{\mathrm{cap}} = 3\ \mathrm{g}$ synthetic rubber stoppers. Including the $m_{\mathrm{fill}} = 3\ \mathrm{g}$ of solution leads to a total system mass of $m_{\mathrm{total}} = 15\ \mathrm{g}$. The 95 wt% solution has a solids mass of $m_{\mathrm{solids}} = 0.05 m_{\mathrm{fill}}$, so $m_{\mathrm{solids}} = 150\ \mathrm{mg}$. Throughout the lyophilization process, water sublimates out of the vial until a porous, solid cake remains with $\approx$ 2 wt% water. This final residual moisture content is defined with respect to the solids mass which leads to a desired final mass of water of $m_{\mathrm{water,end}} = 0.02 m_{\mathrm{solids}}$, so $m_{\mathrm{water,end}} = 3\ \mathrm{mg}$. Therefore, to detect the endpoint of this process, the final mass measurement of the 15 g assembly must be accurate to $\mathcal{O}(1\ \mathrm{mg})$ which requires a precision of 1 part in 10,000.

The images or videos of the sensor captured by a camera can be mapped back to physical lengths by rescaling the image based on the known edge length of the fiducial markers. For a view centered on a 10R vial with a frame size double the vial mouth diameter, a standard HD camera with a 1920 px × 1080 px resolution will have a 70 mm × 40 mm view available. Assuming that the camera can resolve distances in images to $\mathcal{O}(1\ \mathrm{px})$ leads to an expected physical resolution of $\approx$ 37 μm. However, instead of capturing a single image to estimate the optical fiducial positions, a 10 second video can be captured at 30 frames per second. This video will observe small oscillations in the fiducial marker positions, providing $\sqrt{30 \times 10} \approx 20\times$ improvement in the resolution of the average position of the optical fiducials per the Central Limit Theorem. Overall, this optical measurement system is expected to resolve fiducial marker motions down to $\Delta d_{\mathrm{min}} \approx 2\ \mu\mathrm{m}$. Therefore, a sensor with a desired $\Delta m_{\mathrm{min}} = \mathcal{O}(1\ \mathrm{mg})$ must have a compliance of at least 0.5 mm/g.

The sensors presented in this paper were designed with a target compliance of at least 1 mm/g to provide a 2× margin above the detection limit while still allowing for flexibility in the position of the sensor within the frame of the camera.

3. Mechanical concept

The sensor developed uses two helical spring wires to hold a suspended load, as shown in Fig. 2. Each wire has one end anchored and one end free, connected by a helical arm. The free end has a crook that holds a basket carrying the suspended vial load and an extended sensing arm that amplifies the spring wire motion and moves in a plane parallel to the top of the vial.

The curved arm of the helical spring wire uses torsional loading efficiency to increase system sensitivity while maintaining a small footprint. This geometry is also simple to manufacture using conventional wire bending techniques. The vertical deflection of the free end of each

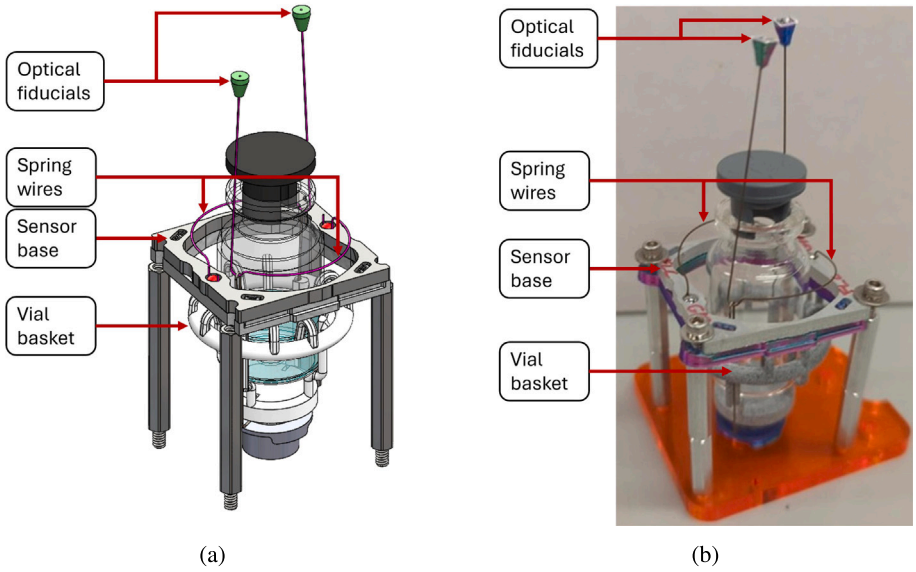

Fig. 1. The vial mass sensor assembly consists of the spring wires, the sensor base in which the wires are mounted, the vial basket that holds the vial, and the optical fiducials that are tracked by a camera.

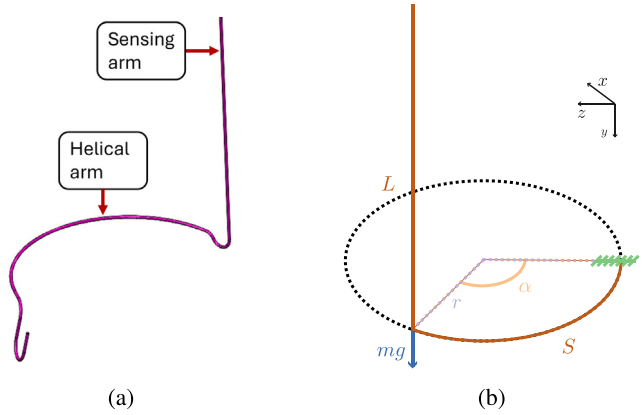

Fig. 2. Fig. 2(a) shows the deflecting helical spring wires used to monitor the vial mass change. This wire has an extended sensing arm to amplify its deflection motion. Fig. 2(b) models the deflection of the helical arm as a curved cantilevered beam with out of plane loading at its free end.

wire can be predicted using a model for the deflection of a curved beam experiencing out-of-plane loading as derived by [19]. Fig. 2(b) presents the model for this deflection, with the final result from a derivation in Appendix A.1 being

$$\delta_{\text{vertical}}(m,\alpha) = \underbrace{\frac{32mgr^3}{\pi E d^4}(\alpha - \sin(\alpha)\cos(\alpha))}_{\delta_{\text{bending}}} + \underbrace{\frac{8mgr^3}{\pi G d^4}(6\alpha - 8\sin(\alpha) + \sin(2\alpha))}_{\delta_{\text{torsion}}} \tag{1}$$

where r is the beam's radius of curvature, E is the beam's elastic modulus, d is the wire diameter, G is the beam's shear modulus, m is the mass supported, g is the local gravitational constant, L is the length of the sensing arm, and α is the total angle subtended of the helical arm. This deflection is decomposed into the curved beam's bending, δ_{bending}, and torsional, δ_{torsion}, components.

This analysis shows that the vertical deflection is expected to be linear with the supported mass. Eq. (1) demonstrates that the spring

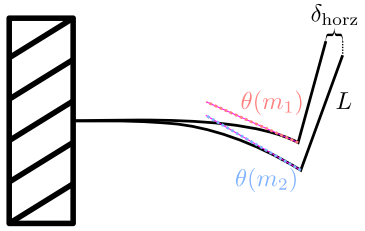

Fig. 3. The changing loading condition m_i on a cantilevered beam changes the induced slope at the end. This slope change can be detected as a displacement, δ_{horz}, of the end of an extended sensing arm of length L mounted perpendicular to the end of the beam.

deflection has a power relationship with the wire diameter and the helical arm's radius of curvature. Thus, these parameters serve as the main driving tools in designing the wires for these springs. Decreasing the wire diameter creates the largest potential increase in deflection, but this strategy is limited by keeping the wire in its elastic deflection regime. Additionally, a thinner wire can be more difficult to mount rigidly into a fixed base, which is required to create the cantilevered beam condition. The wire chosen for this system has a 0.014 in (0.36 mm) diameter to balance this preference for a thinner wire and the requirement of a thick enough wire for repeatability.

Although Eq. (1) provides the vertical deflection at the free end of the spring wire's helical arm due to gravity, this deflection can be difficult to measure for sets of vials in an array. Thus, an extended vertical sensing arm is added to the free end of the helical arm. As the tip of the helical arm deflects downward, it also experiences a slope change that is amplified by the perpendicular sensing arm, as illustrated in Fig. 3. The bending and twisting slopes at the free end of the helical arm are calculated from (Eq. (2) in [20])

$$\begin{aligned}\theta_{\text{bending}} &= \frac{mgr^2}{EI}(C_2\cos(\alpha) - C_1\sin(\alpha)) \\ \theta_{\text{torsion}} &= \frac{mgr^2}{EI}(C_1\cos(\alpha) + C_2\sin(\alpha))\end{aligned} \tag{2}$$

where the specific definitions for the coefficients C_1 and C_2, which depend on the subtended arc angle α, are in Appendix A.1.

The bending slope creates motion in the direction tangent to the helical arm at its end, whereas the twisting slope creates motion perpendicular to the helical arm at its end. Thus, because these motions

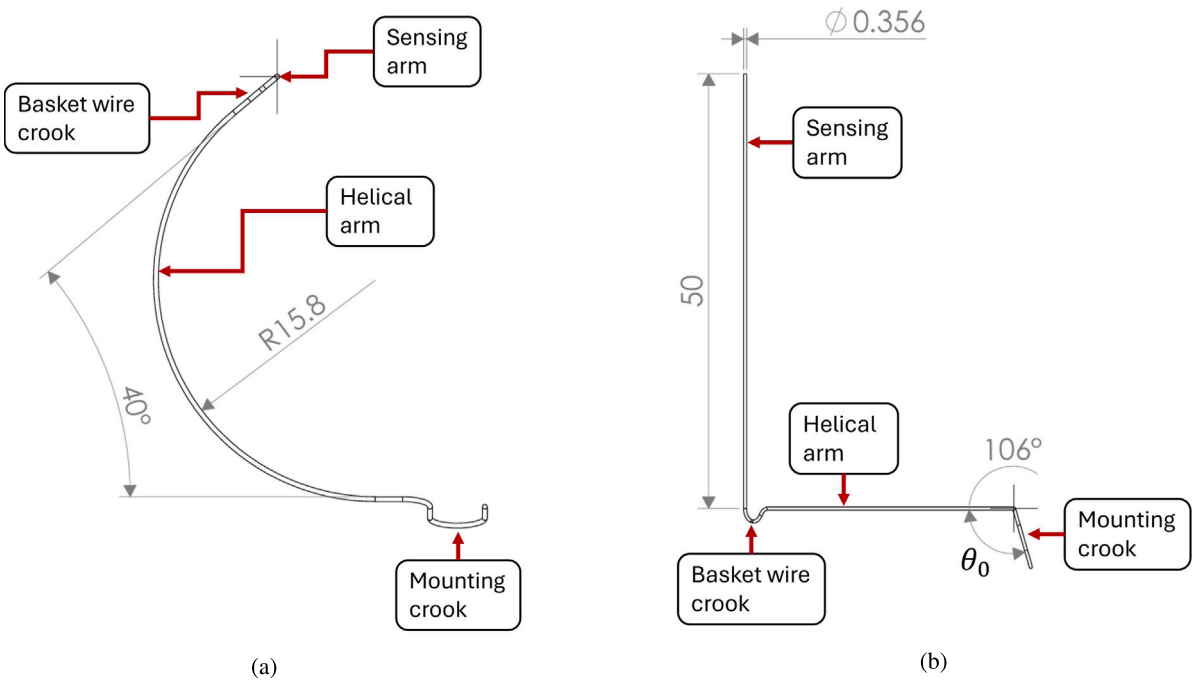

Fig. 4. Fig. 4(a) shows a top view and Fig. 4(b) shows a side view of the spring wire with key dimensions used in the sensors built for this work.

act perpendicularly to each other, the net displacement of the sensing arm tip is the square root of the sum of the squares of each of these induced slope motions. The ratio between this displacement and the load provides the compliance of the sensing wire,

$$C_{\text{horz}} = \frac{\delta_{\text{horz}}}{m} = \frac{L\sqrt{\theta^2_{\text{bending}} + \theta^2_{\text{torsion}}}}{m}, \tag{3}$$

which is used to predict the motion of the sensor when the loaded mass changes. The full calculation for motion of an optical fiducial mounted to the end of the sensing arm given a change in mass is shown for the wire system example developed for this work in Table 2 in the appendix.

4. Prototype system design and key elements

The developed mass sensing system, shown in Fig. 1, consists of four main subsystems: the spring wires, the sensor base, the vial basket, and the optical measurement system. The optical measurement system includes the optical fiducials mounted on the ends of the spring wires and the optical sensor that measures the positions of these fiducials. In this sensor, the optical fiducials are AprilTags and the optical sensor is a digital camera.

4.1. Spring wire

Fig. 4 shows the key dimensions used in this application for the spring wire shown in Fig. 2(a). The spring wire consists of a deflecting helical arm, an extended sensing arm used to amplify the spring deflection and change the motion plane to be parallel to the top of the vial, a mounting crook used to attach the spring wire to the sensor base, and a basket wire crook from which the vial basket is suspended. Corresponding curved elements on the spring wire's basket wire crook and the wires extending from the vial basket enable rolling contact at their interface to prevent sliding between the wires, thereby improving repeatability while minimizing the generation of particulate contaminants. The spring wires used in this work are made from 17-7 PH stainless steel with a CH900 precipitation hardening. The wires were bent by Springfield Spring & Stamping in Bristol, Connecticut.

The full mass of the vial plus the product causes the helical arm to experience a large deflection and changing moment arm, which is necessary to achieve the desired sensitivity. The wire is preloaded so that the helical arm is horizontal at the end of drying to provide the longest moment arm and therefore the greatest sensitivity when the water mass is minimal. This preload is achieved by bending the wire mounting crook in a plane offset from perpendicular to the helical arm, as shown by θ_0 in Fig. 4, and is calculated in Appendix A.2.

At least two wire supports are needed to keep the vial level in the sensor while maintaining access to its top, which must remain clear to allow vial capping. These wires are positioned in axially symmetric positions to avoid biasing the vial in any direction. While more wires can improve vial stability, they also distribute the load of the vial and will each deflect less, reducing overall system sensitivity.

4.2. Sensor base and assembly

Fig. 5(a) shows the sensor base that provides the resistant forces and moments needed to keep one end of the wire fixed while the other end deflects under the vial and product weight. All of the base features are 2D to enable rapid and large-scale manufacturing with methods like laser cutting. The sensor bases used in this work were laser cut by SendCutSend from 0.125 in thick 5052 H32 Aluminum.

The wire mounting uses a press-fit ball to secure the wire to the base as shown in Fig. 6. The ball press fit cutouts are positioned axisymmetrically about the center of the wire base to ensure that the vial is located centrally in the base. This arrangement also makes the basket hanger crooks parallel to each other, allowing the interface with the basket wires to achieve the designed rolling contact rather than stochastic sliding.

The sensor base assembly process requires the fixturing shown in Fig. 5(b) to constrain the sensing wire and ball plug degrees of freedom to ensure consistent wire positions that do not bias the sensor. A laser cut positioning assembly locates the sensor base under an arbor press, while 3D printed holders constrain the wire and the ball plug to prevent components from shifting during the press operation. Motion of either component would alter the wire preload angle and cause the vial to tilt in the sensor, leading to frictional drag that reduces the repeatability of the measurement.

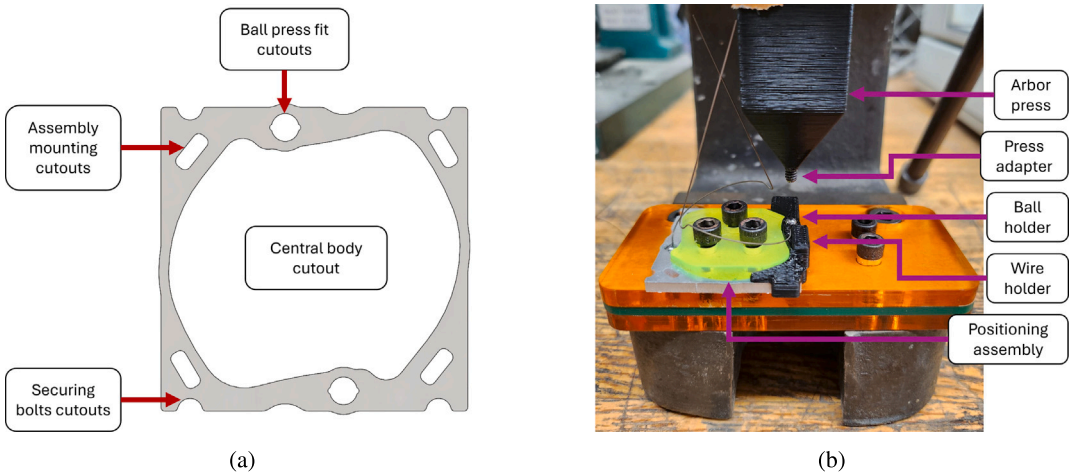

Fig. 5. Fig. 5(a) shows the sensor base, which has ball press fit cutouts for mounting sensing wires, a central body cutout for the vial to move through, assembly mounting cutouts to add the sensors to an array, and securing bolts cutouts for holding the sensor in place. The sensing wires are mounted with the fixturing shown in Fig. 5(b).

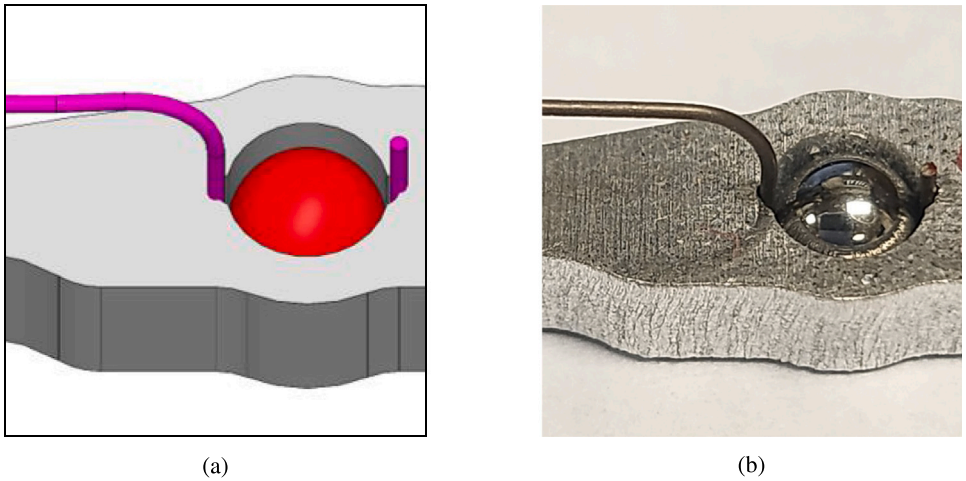

Fig. 6. Fig. 6(a) shows the model and Fig. 6(b) shows the as built ball plug press fit mounting used to mount the spring wires to the wire base. This mounting provides a rigid support for the deflecting spring wire.

4.3. Vial basket

The vial basket, shown in Fig. 7(a), holds the vials in the sensor. The basket is suspended by its basket wires from the basket wire crooks on the sensing wires. The basket wire holders keep one degree of freedom available to accommodate differential thermal expansion. Elastically averaging arms securely hold the vial in the center of the basket, preventing parasitic vial movement or tilt. The support ring helps the system resist the forces created by vial loading and capping. The positioning posts locate the bottom of the vial in the vial basket. The base counterweight improves system stability by lowering the center of mass of the vial basket assembly below the basket's tilt axis. The vial baskets for this work were multi-jet fusion printed from HP PA 12 with an 80 μm layer height by the Protolabs Network by Hubs.

The vial and basket assembly must remain upright to prevent components from rubbing against each other. The axis of rotation for vial tipping is defined by the line between the two basket wire and basket wire crook interfaces, while the spring system center of stiffness is the center of the two helical arms. The vial basket assembly is stable if its center of mass is below both the tilt axis and the center of stiffness because off-axis loading will create a restoring force that straightens the vial, as shown in Fig. 7(b). Positioning the center of mass of the vial and vial holding structure above the spring system center of stiffness or the mounting rotational axis, like examples in [21], leads to significant stability issues.

4.4. Optical sensor

The change in the position of the tip of the sensing arm during the sublimation process is measured by a camera. The reliability of this sensor depends on the ability of the camera to locate the tip of the arm in each image or video. To improve this process, an AprilTag is mounted on the end of each sensing arm, as shown in Fig. 8(a), by gluing the AprilTag to a plastic nub that is then glued on the wire. The Loctite Ultra Gel Control Super Glue used exhibited no off-gassing when placed in the vacuum chamber. These optical fiducials have robust utilities for detection built into programming languages like MATLAB and Python [22]. Fig. 8(b) shows the typical motion that is detected by the camera when the vial deflects under a changing load.

5. Testing hardware

5.1. Automated calibration system

An automated offline testing system, shown in Fig. 9, was built to evaluate the spring wire sensor before using it in a lyophilizer. The sensor is placed on an analytical balance (Mettler Toledo AG204 DeltaRange) to directly measure the mass changes in the vial and a Canon Rebel T7i with an 18-55 mm lens is used to capture the AprilTag positions during the tests.

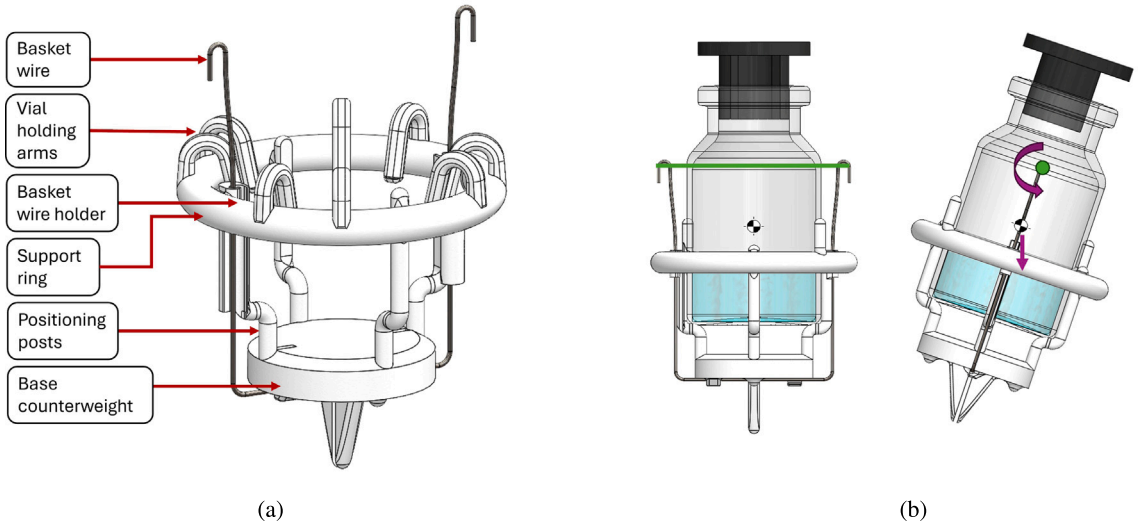

Fig. 7. Fig. 7(a) shows the wire basket assembly is used to hold vials in the sensor. Fig. 7(b) shows the rotational axis of the vial basket that goes through the mounting points on the basket wire. If the center of mass of the vial basket assembly is below this axis when the basket tilts, then gravity creates a restoring moment which returns the vial basket assembly to an upright state.

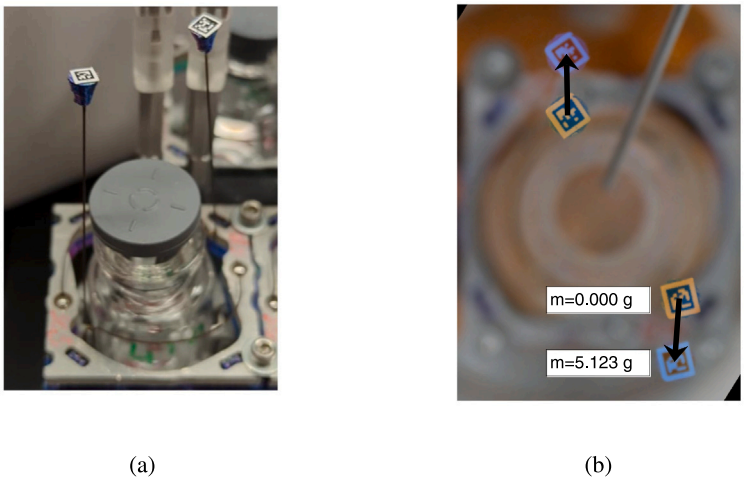

Fig. 8. Fig. 8(a) shows the AprilTags on the ends of the spring wire sensing arms. Fig. 8(b) shows the typical displacement of these AprilTags after adding water. This figure is generated by overlaying an image of the sensor at 0 g and 5 g, with differences between the two images highlighted in orange (first image) and blue (second image). (For interpretation of the references to color in this figure legend, the reader is referred to the web version of this article.)

Since the springs deform elastically, the motion when adding or subtracting water is expected to be symmetric, so either method could be used for the calibration tests. These calibration tests use a peristaltic pump (Masterflex 7521-40) to add 10 g of water to the vial in 0.5 g increments through a needle placed above the vial. After each incremental addition, the vial is given four minutes to settle before a 10 s video is recorded to measure the AprilTag positions. Each calibration test takes 90 min.

5.1.1. Offline data pre-processing

The model described in Section 3 requires a reference mass, m_{ref}, to define the reference positions, $(x_{\text{ref}}, y_{\text{ref}})$, for each AprilTag from which the deviation, δ_{horz} is measured. For each calibration test, the mass of the empty vial plus the basket was chosen as m_{ref}. Appendix B contains a description of how the `readAprilTag()` function in MATLAB was used to convert the collected videos into measured deviations.

5.2. Lyophilization hardware

After calibration, the sensors are assembled into the array shown in Fig. 10(a) and loaded with vials that are then lyophilized in a custom aluminum vacuum chamber. These sensors are sufficiently affordable (~$10 each) for every vial lyophilized in this work to be placed in a sensor. The vacuum chamber, shown in Fig. 10(b), is built around a magnetic levitation motion system from Planar Motors Inc. in Richmond, British Colombia, Canada. This system enables precise positioning of the sensor array under the camera so that each sensor can be measured through an acrylic window, as shown in Fig. 11(a).

Vials are prepared for lyophilization by first filling them with 3 mL of an aqueous solution with 5 wt% of a 50:50 mixture of sucrose (Sigma-Aldrich) and mannitol (Sigma-Aldrich) before freezing them overnight in a −40°C freezer. During transfer between the freezer and the vacuum chamber, the vials are placed in liquid nitrogen and allowed to equilibrate so that they remain well below 0 °C. During the lyophilization experiment, vacuum pressure was maintained below 6 Pa as monitored by both Pirani (Agilent Varian PCG-750) and diaphragm (MKS Baratron Type 626) pressure gauges. Vials are dried via radiation, and the process is controlled by maintaining the chamber wall temperature at 25 °C. At the end of a lyophilization experiment, the vials were capped under vacuum and removed from the chamber.

The vacuum chamber includes both Pirani and diaphragm pressure gauges because they are used for batch-level endpoint detection during

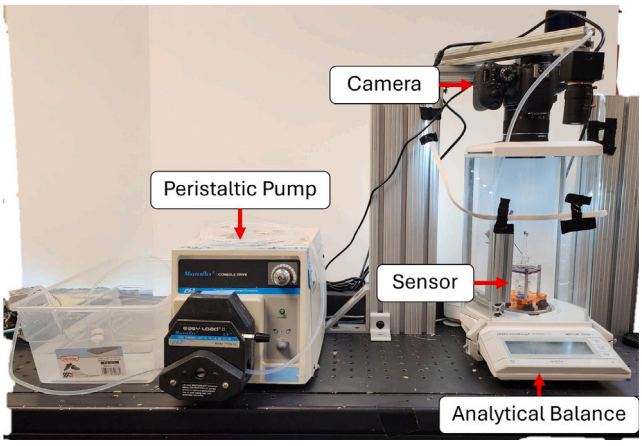

Fig. 9. The system for calibrating the spring wire sensor uses an analytical balance to provide the ground truth measurements of vial mass changes. The mounted camera records the tag positions as the peristaltic pump intermittently adds water to change the mass in the vial.

lyophilization [7]. The former is sensitive to which gas is in the headspace because it uses thermal conductivity to infer pressure while the latter measures a physical deflection from pressure. The ratio of these measurements is 1.6 when the rarefied gas is mostly water vapor, which has a higher thermal conductivity than air. Once the source of water vapor is depleted by sublimation of the bulk ice in the vials, the ratio returns to 1. This pressure ratio test is used in Section 7.2.1 to validate the endpoint detected by the mass sensors.

5.2.1. Online data collection pre-processing

During the lyophilization experiments, the motion system cycles the array of sensors between five positions, at each of which two full sensors are visible. Viewing two sensors simultaneously requires a decrease in camera zoom relative to the offline calibration test, but it halves the total time required to measure the full array, increasing the measurement density during an experiment. After moving between positions, the sensors are given 90 s to stabilize before a 15 s video is recorded. The videos are analyzed using similar code to that described in Appendix B. As in Section 5.1.1, reference positions for the assembled array are collected in an experiment where each support is loaded with an empty vial.

Because the sensor array moves relative to the camera, deviations calculated in the coordinate system of the camera may not match those in the coordinate system of the sensor. A coordinate system for the sensors is defined using the reference AprilTags shown in Fig. 11(b) such that the centroid of the reference AprilTags is at $(0,0)$ and the two reference tags fall on the y-axis. In practice, some reference AprilTags became loose in their fixtures and no longer provide a consistent position. When this occurred, this AprilTag was ignored, the centroid of the stable tag was set to $(0,0)$ and no rotation correction was performed.

6. Model fitting and performance evaluation

This section describes the calibration data analysis and the evaluation of each sensor's performance. A set of $N_{\text{sensor}} = 10$ sensors were calibrated $N_{\text{cal}} = 4$ times over a range of $m_{\text{water}} \in [0\,\text{g},\ 9.5\,\text{g}]$ per Section 5.1. The actual measured mass, $m_{\text{meas}} \in [14.5\,\text{g},\ 24\,\text{g}]$, represents the total mass supported by the spring wires, including the vial and the basket assembly. Even though Section 3 details that the response of the spring wires to changes in mass is expected to be linear, polynomial models of order $N_P \in \{1,2,\ldots,6\}$ were all tested to account for possible nonlinear effects. Additionally, as described in Section 5.1.1, the deviation in mass is calculated from the reference mass m_{ref}. Therefore, the models considered in this paper take the form:

$$\hat{m}_i = f(d_i;\boldsymbol{p}) = m_{\text{ref}} + \sum_{j=0}^{N_P} p_j (d_i)^j \tag{4}$$

While the full set of N_{fit} pairs of $\{d_i, m_i\}$ data is used to determine the optimal $\hat{\boldsymbol{p}}$, the set of N_{test} pairs of $\{d_j, m_j\}$ used to evaluate the model is smaller to match the mass change range of interest.

The primary metric used for comparing different models, such as different order fits and different $\hat{\boldsymbol{p}}$, is the root mean square error,

$$\text{RMSE} = \sqrt{\frac{\sum_{j=1}^{N_{\text{test}}} \left(m_j - f(d_j;\hat{\boldsymbol{p}})\right)^2}{N_{\text{test}}}}, \tag{5}$$

where the $j = \{1,2,\ldots,N_{\text{test}}\}$ indexes over the set of $\{d_j, m_j\}$ pairs are associated with model testing and not model fitting. The datasets associated with the N_{fit} pairs of $\{d_i, m_i\}$ data are used to determine $\hat{\boldsymbol{p}}$.

6.1. Dataset selection

The range of data relevant to evaluating models is the set of masses over which the vials are expected to vary during the lyophilization process described in Section 5.2. In the lyophilization experiments, a 9.4 g vial is filled with 3.0 g of aqueous solution, partially stoppered with a 3.6 g cap, and placed in a 2.2 g basket, resulting in a full supported mass of 18.2 g. Throughout the drying process, the water, representing the vast majority of that 3 g solution, sublimates away, such that the minimum mass supported is 15.2 g. Thus, the nominal range of mass supported is $m_{\text{supported}} \in [15.2\,\text{g},\ 18.2\,\text{g}]$. This nominal range was expanded by 0.5 g on each end to $m_{\text{supported}} \in [14.7\,\text{g},\ 18.7\,\text{g}]$ to account for empirically measured variation in masses (Appendix C).

When selecting a range of data to use for fitting the coefficients of the model, it is desirable to maximize the number of observations used. However, not all of the data collected during the calibration are usable because some sensor assemblies bottom-out in the testing fixture after more than 8.5 g of water have been added to the vial (total supported mass, $m_{\text{supported}} > 22.5\,\text{g}$). Therefore, only the data from the range $m_{\text{supported}} < 22.5\,\text{g}$ are used for fitting the coefficients.

6.2. Per sensor calibrations

Each sensor is initially characterized by applying the following two procedures to the N_{cal} available for each sensor. These calibrations characterize the variation of each sensor assembly across replicates.

6.2.1. Testing and fitting procedures

Withholding a subset of the collected data to test a model is standard practice in the machine learning literature as a strategy to reduce the risk of over-fitting and more accurately estimate the true performance of a model [23].

This paper implements a 1-dataset holdout method where, for each of the N_{sensor} sensors, the fit coefficients $\hat{\boldsymbol{p}}$ were fit on $(N_{\text{cal}} - 1)$ of the datasets, and the testing performance was measured on the remaining dataset. This procedure was repeated for each dataset to estimate the distribution of performances likely to be observed.

6.2.2. Online parameter refinement

During a lyophilization experiment, the initial mass of the filled vial and the sensor's starting AprilTag positions are available; however, this single observation, (m_o, d_o), is not sufficient to uniquely determine all elements of $\hat{\boldsymbol{p}}$. However, the maximum a posteriori method (MAP) can be used to combine this online measurement with a distribution for $\hat{\boldsymbol{p}}$ estimated from the offline calibration data. This new $\hat{\boldsymbol{p}}_{\text{MAP}}$ is defined as

$$\hat{\boldsymbol{p}}_{\text{MAP}} = \arg\max_{\boldsymbol{p}} \ \mathbb{P}(m_o, d_o|\boldsymbol{p})\,\mathbb{P}(\boldsymbol{p}), \tag{6}$$

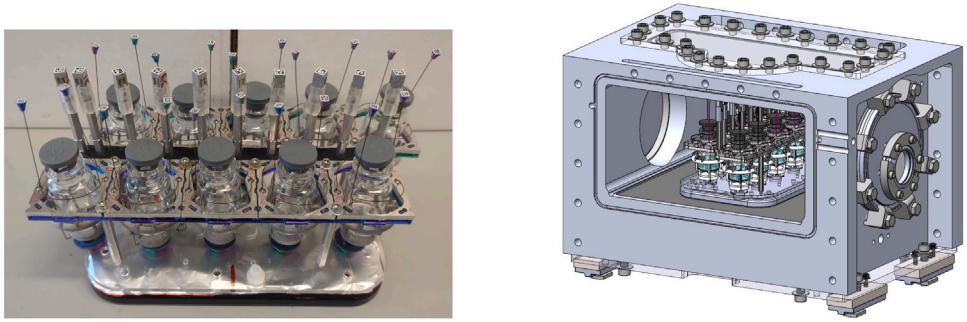

(a) (b)

Fig. 10. Fig. 10(a) shows the as-built sensor array loaded with vials. Fig. 10(b) shows a CAD model of the sensor array inside the vacuum chamber.

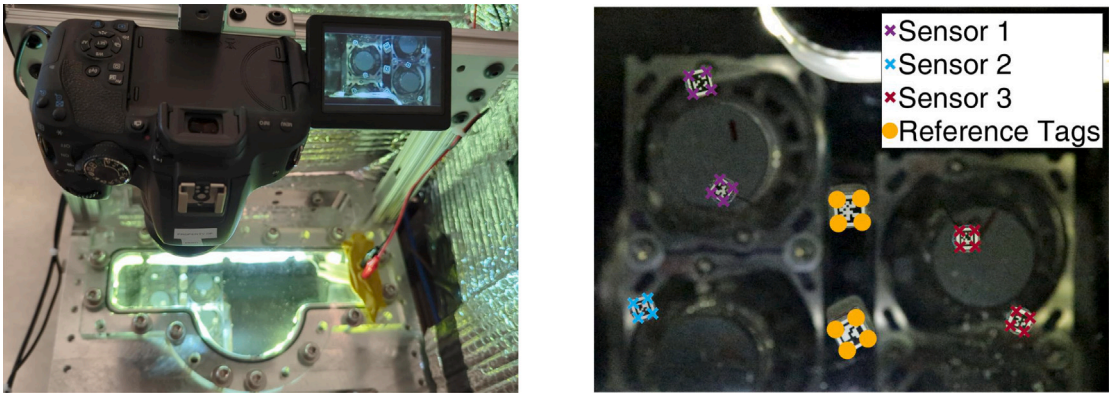

(a) (b)

Fig. 11. Fig. 11(a) shows the assembled sensor array inside the vacuum chamber. Internal LEDs are used to provide consistent illumination for the AprilTags. Fig. 11(b) shows an example image captured by this hardware with the corners of each AprilTag highlighted. (For interpretation of the references to color in this figure legend, the reader is referred to the web version of this article.)

and determined by optimization of the product of the two functions, $\mathbb{P}(m_o, d_o|\boldsymbol{p})$ and $\mathbb{P}(\boldsymbol{p})$. The first term is the likelihood function which is the likelihood of observing the pair (m_o, d_o) for fixed $\boldsymbol{p}$. In the absence of any other information, it is common to assume this function follows a normal distribution around 0 with some σ_E [24],

$$\mathbb{P}(m_o, d_o|\boldsymbol{p}) \sim \exp\left(-\frac{\left(m_o - f(d_o;\boldsymbol{p})\right)^2}{2\sigma_E^2}\right) \tag{7}$$

Here, because the sensors were designed to be accurate to $\mathcal{O}(1\,\text{mg})$, a value of $\sigma_E = 5\,\text{mg}$ was chosen. The results are not sensitive to the choice of σ_E, as shown in Appendix D.

The second term in Eq. (6) is an estimated, multi-variate distribution of $\boldsymbol{p}$ that underlies the process which is an estimate of how much each element of $\boldsymbol{p}$ can vary in a good fit. This term is commonly simplified with two assumptions: (1) each element of $\boldsymbol{p}$ is independent and (2) the distribution of each element p_i is Gaussian [24]:

$$\mathbb{P}(\boldsymbol{p}) \sim \prod_{i=0}^{N_P} \exp\left(-\frac{(p_i - \mu_{p_i})^2}{2\sigma_{p_i}^2}\right). \tag{8}$$

Estimates of μ_{p_i} and σ_{p_i} for each element of $\boldsymbol{p}$ must exist to evaluate this equation. The strategy described in Section 6.2.1 describes how a single optimal value of $\hat{\boldsymbol{p}}$ is computed by concatenating $(N_{\text{cal}} - 1)$ of the datasets available for a sensor. To estimate μ_{p_i} and σ_{p_i}, the same model can additionally be fit to each of the $(N_{\text{cal}} - 1)$ datasets separately, and then the mean and standard deviation of each element of $\boldsymbol{p}$ is computed. These extra fit $\boldsymbol{p}$ parameters are only used to estimate the distribution of $\boldsymbol{p}$ and are not used directly for any model evaluation.

With these $\mathbb{P}(m_o, d_o|\boldsymbol{p})$ and $\mathbb{P}(\boldsymbol{p})$ defined, for any new observation of (m_o, d_o), there exists a function defined over $\boldsymbol{p}$ that can be maximized per Eq. (6) to obtain the new $\hat{\boldsymbol{p}}_{\text{MAP}}$. This new $\hat{\boldsymbol{p}}_{\text{MAP}}$ balances both information about the expectation for where the true value should be and the knowledge that (m_o, d_o) was observed.

6.3. Sparse calibration

It is desirable to reduce the calibration time required for each sensor. The simplest strategy is to calibrate a subset of sensors and use the average calibration coefficients on the remaining sensors. To avoid overfitting, the sensors are split into even- and odd-indexed subsets. When one set is held out for testing, the other is used to fit the average coefficients. This procedure can also be refined with a MAP update as μ_{p_i} and σ_{p_i} can be computed directly from the data for the sensors that are used for fitting. Note that the σ_{p_i} calculated here will be larger than in the previous section because it captures the variation across sensors rather than within replicates of a single sensor. Section 7.1.2 shows that this average coefficient strategy does not perform sufficiently well, so individual sensor calibration is required.

To evaluate the sensitivity of each sensor's performance to the amount of calibration data used, fits are made using a variable number of data points, N_{sparse}, from a single calibration replicate. When $N_{\text{sparse}} < N_{\text{fit}}$, the points closest to the boundary are included in the fit because they estimate the linear coefficient most accurately. To estimate the distribution of each sensor's performance with this strategy, each of the N_{rep} datasets per sensor is held out and tested against the remaining $(N_{\text{rep}} - 1)$ datasets. To refine this procedure with an MAP update, the $\hat{\boldsymbol{p}}$ calculated from the N_{sparse} data can be used as an estimate of μ_{p_i}. However, σ_{p_i} cannot be calculated because there is no replicate data available. The same even- and odd-indexed splitting

Table 1
Comparison of the predicted and observed values for key performance parameters. The vertical compliance of the sensors was measured by replacing the camera in the automated testing setup with a laser displacement sensor (Keyence CL-L070).

Parameter	Symbol	Predicted	Measured
Vertical Compliance	C_{vert}	0.56 $\frac{\text{mm}}{\text{g}}$	0.62 ± 0.02 $\frac{\text{mm}}{\text{g}}$
Horizontal Compliance	C_{horz}	1.21 $\frac{\text{mm}}{\text{g}}$	1.27 ± 0.12 $\frac{\text{mm}}{\text{g}}$
Minimum Resolvable Distance	Δd_{min}	2 μm	2.31 ± 0.93 μm

described above is applied so that the set of sensors not being tested can be used to estimate σ_{p_i}. Specifically, σ_{p_i} is calculated for each of those sensors and the average value is used when the MAP update is applied.

7. Results

Table 1 shows that the vertical compliance of the helical arm and the horizontal compliance of the sensing arm agree with the values predicted in Section 3. This result demonstrates that this sensor design creates the expected motion required to measure the mass of vials in a range relevant to the lyophilization process. The minimum resolvable AprilTag motion Δd_{min} presented in Section 2.1 is empirically measured as $\Delta d_{\text{min}} = 3\sigma_{\mu_d}$. The standard deviation of μ_d, characterizes the magnitude of the observed oscillation in the position of the AprilTag and the 3σ cutoff provides the minimum difference two measurements must have for a 99% certainty that they are distinct. The expected minimum RMSE of the sensors, given by $\frac{\Delta d_{\text{min}}}{C_{\text{horz}}}$, is 1.7 mg, which is consistent with the $\mathcal{O}(1\text{ mg})$ target from Section 2.

7.1. Calibration performance

The calibration data were collected using the hardware described in Section 5.1 and analyzed according to the methods in Section 6.

7.1.1. Per sensor calibration performance

Applying the coefficients that were fit with one dataset to that same dataset provides a bound for the best performance that could be observed but over-fits the data. Fig. 12 shows that while linear models perform well, they do not describe the relationship between the vial mass and AprilTag displacement to the precision required in Section 2. If higher order terms are used, as suggested in Eq. (4), the desired accuracy of 2 mg is achieved. There are multiple potential sources of these nonlinear effects, such as deflection in the spring wire between the mounting crook and the helical arm, the constraint on the spring wires imposed by the vial basket, and optical effects from the camera. However, their contributions are sufficiently small that the polynomial terms, rather than explicit modeling, accurately capture them.

The results of applying the cross-validation procedure described in Section 6.2.1 are shown in Fig. 13(a). The calculated RMSE have a mean value of 16 mg and a median value of 13 mg for fits of at least third order, indicating that the 2 mg accuracy found in Fig. 12 is explicitly caused by over-fitting. This increased error is likely caused by small variations in the sensor setup between replicates. This error also overpowers the small performance benefit of increasing the order of the fitting polynomial past second order. However, these small variations can be accounted for in part by using the MAP method in Section 6.2.2. Fig. 13(b) shows that when the MAP procedure is applied, mean and median accuracies of 7.8 mg and 6.5 mg are recovered.

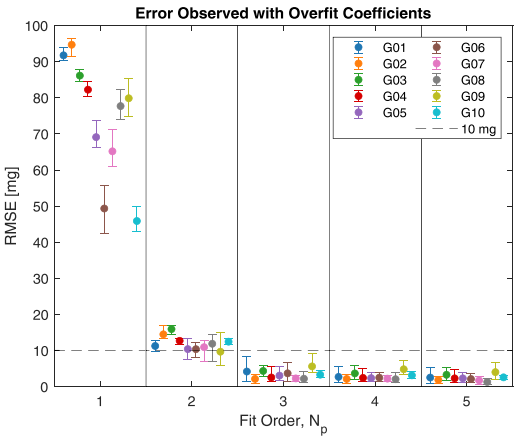

Fig. 12. The calibration data are over-fit to show that the mass measurement error as a lower bound of 2 mg.

7.1.2. Sparse calibration performance

As described in Section 6.3, the simplest strategy to reduce the total calibration time is to calibrate a subset of the sensors and use those coefficients for uncalibrated sensors. This strategy requires all of the sensors to have similar best-fit coefficient values. Fig. 14 shows that the coefficient variation between all ten sensors is small but non-negligible. Fig. 15 shows that applying the average calibration coefficients for the even-indexed sensors to the odd-indexed sensors and vice versa generally results in errors greater than 50 mg. These errors are much larger than those in Fig. 13(a), where each sensor was tested on its own calibration data, indicating that this simple strategy is not sufficient to reduce calibration time. The most likely source of variation in the linear term is the manufacturing tolerance of the spring wires. For example, the ±0.1 in tolerance set by manufacturability considerations on the helical arm radius, r, could result in up to a 0.77 $\frac{\text{mm}}{\text{g}}$ change in the compliance predicted by the modeling in Section 3.

Next, the range of possible N_{sparse} data points were used to estimate calibration coefficients for each sensor, and the results are reported in Fig. 16(a). For all orders of the fitting polynomial, N_P, the error decreases as the number of points increases. However, Fig. 16(b), which shows the performance after including the MAP update, quickly approaches the optimal performance, significantly reducing the required calibration time. For example, a third-order model with a MAP update would achieve a mean RMSE of 17 mg and a median RMSE of 15 mg while only requiring 20 min of calibration time per sensor.

7.2. Online performance

After calibration, the sensors were assembled into an array, and their reference positions were measured in the lyophilization chamber per Section 5.2.1. The consistency of the measured deviation in a single video, as measured by Δd_{min}, increased slightly between the offline and online setups, as shown in Appendix E. However, the motion of the sensor assembly between measurements potentially introduces additional variability to the measured deviation, even after adding the coordinate system correction. This error was quantified by repeatedly measuring and moving the sensor array loaded with empty vials. This test reported a median 3σ limit on the AprilTag deviation from this motion of 48 μm, which dominates the online Δd_{min} of 7.5 μm. Therefore, the expected minimum in situ error increases from $\frac{\Delta d_{\text{min}}}{C_{\text{horz}}} = 1.7\text{ mg}$ to $\frac{48\text{ μm}}{C_{\text{horz}}} = 38\text{ mg}$. Possible sources of this observed in situ hysteresis include shifting of the vial basket and sensing wire interface induced by moving the sensor and the possibility of frictional interfaces being introduced by the assembly of sensors into the array for lyophilization.

The masses reported by the online system were calculated using third-order models. When coefficients were updated using the MAP

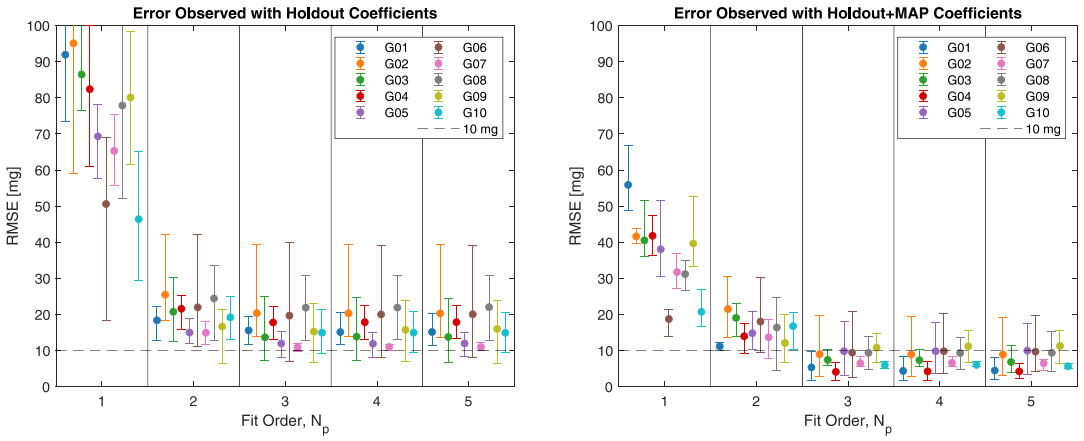

Fig. 13. Fig. 13(a) shows that when cross-validation procedures are observed, the mean error rises to 16 mg. Fig. 13(b) shows that a MAP update of the parameters reduces the mean error to 7.8 mg. The error bars span the minimum and maximum RMSE observed at a given condition.

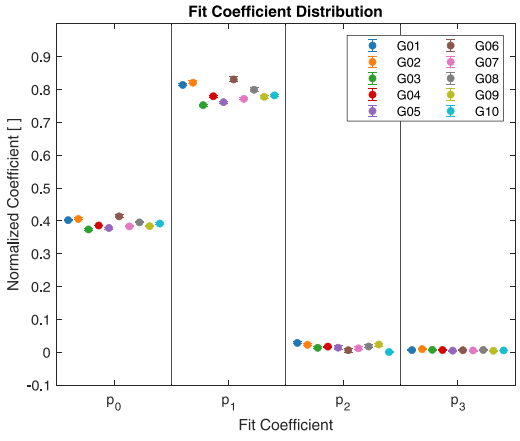

Fig. 14. The distribution of each normalized calibration coefficient, p_i, is tight when m_i and d_i are rescaled to $[0, 1]$.

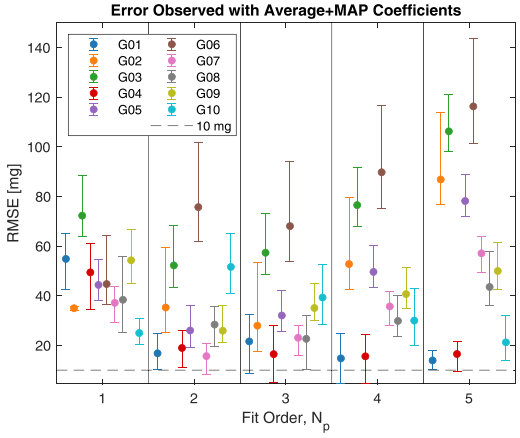

Fig. 15. Despite the apparently small variation, the high sensitivity of the system leads to the poor transferability and, over-fitting occurs at higher orders.

procedure, the values of σ_{p_i} and μ_{p_i} were estimated using all available calibration data for each support. When coefficients were not updated, all available calibration data was used to fit $\hat{p}$ per support.

The collected mass vs. time data can also be used to estimate the current sublimation rate using numerical differentiation. Because numerical derivatives are sensitive to noise, the mass trajectories are first smoothed using a 45 min backwards simple moving average window. The derivative was then calculated at each point using first order backwards difference approximations. The use of backwards windows allows these methods to be directly applied to online data as it is collected.

7.2.1. *Single vial lyophilization*

The batch drying endpoint from the pressure ratio test described in Section 5.2 can be used to characterize the endpoint reported by the mass sensors if a batch size of one vial is used. Fig. 17 shows that the endpoint detected by the pressure ratio test is consistent with the flattening of the estimated mass vs. time trajectory. To match the pressure ratio test, the senor's endpoint is defined as the time at which the derivative of the mass trajectory is $> -0.5\ \frac{\text{mg}}{\text{min}}$.

7.2.2. *Multi-vial lyophilization*

The lyophilization experiment was repeated with an array of ten vials, each in their own sensor. In this experiment, vial 6 was loaded without any solution as an internal standard. To reduce the sublimation rate of vial 8, the frozen product was partially detached from the vial wall after its temperature was reduced to −200 °C. The pressure ratio and mass trajectories in Fig. 18 show that the pressure ratio goes to 1 when the final mass sensor reports that its vial has finished drying. These results demonstrate that the mass sensors can determine which vial limited the process by providing per vial resolution on sublimation rate and drying endpoint.

While the gradient based drying endpoint detection method does not require accurate mass estimation, the accuracy of the final mass recorded can be used to compare the performance of the sensors online to their offline performance from Section 7.1. To test these mass sensors over a range of conditions, the ten sensor lyophilization experiment was repeated with several different drying times to generate a range of final masses, and the final vial masses were measured on a balance after they were removed from the lyophilizer. Fig. 19 shows how accurate these reported final mass values are on a per sensor basis.

Sensor G01 shows much higher final mass error than the other sensors because its vial basket contacts the sensor base before the sublimation for its vial ends, so the measured final mass is lower than the sensor reports. The remaining nine sensors have a mean RMSE of 78 mg and a median RMSE of 50 mg when the offline coefficients are applied directly. If the MAP procedure is applied to update coefficients using the known initial mass, these errors inflate to an average value

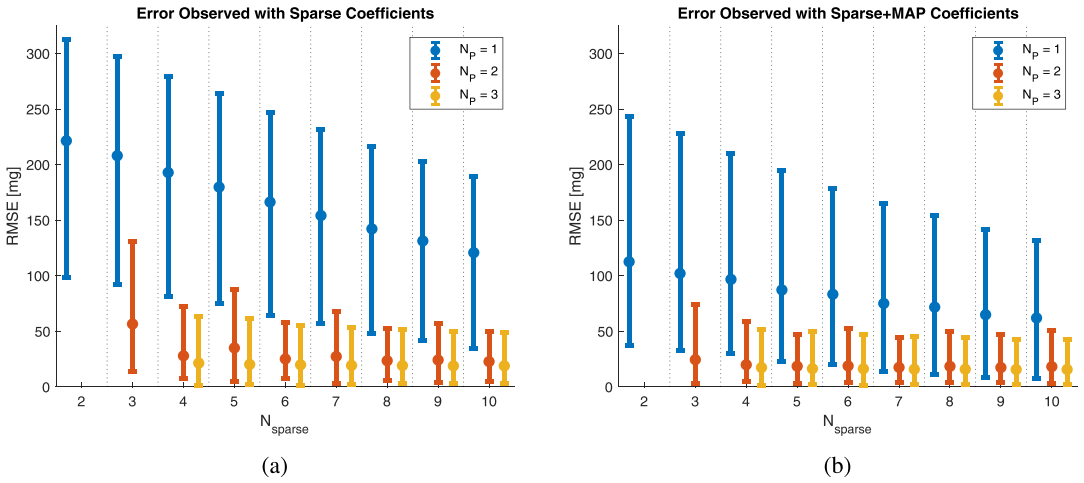

Fig. 16. Root-mean-squared error for a range of values of N_P and N_{sparse}: (a) using only offline data and (b) improvement made with the 1-point MAP. The error bars spans the maximum and minimum error observed for all $N_{\text{sensor}} = 10$ supports at the given condition.

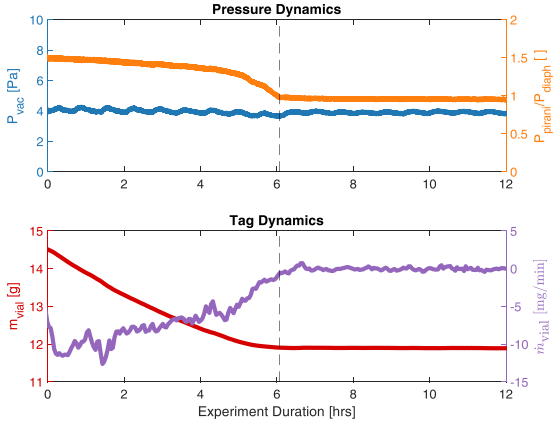

Fig. 17. The end of drying behavior detected by the pressure ratio test and the mass sensor are consistent. The mass trajectory was smoothed using a 45 min backwards simple moving average window to improve stability. The vertical dashed lines mark the end of drying as detected by the pressure ratio test.

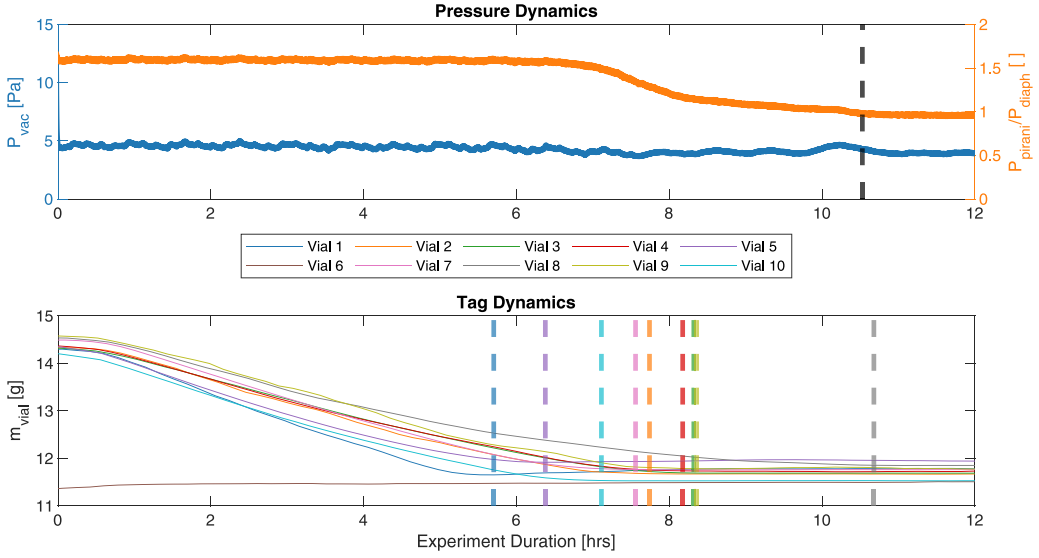

Fig. 18. The lyophilization experiment with ten mass sensors shows that the pressure ratio test is able to detect the endpoint of primary drying for the final vial in the system, but the mass sensors provide more detailed feedback. The black dashed line marks the end of primary drying as detected by the pressure ratio test, and the colored dashed lines mark the per-vial drying endpoints.

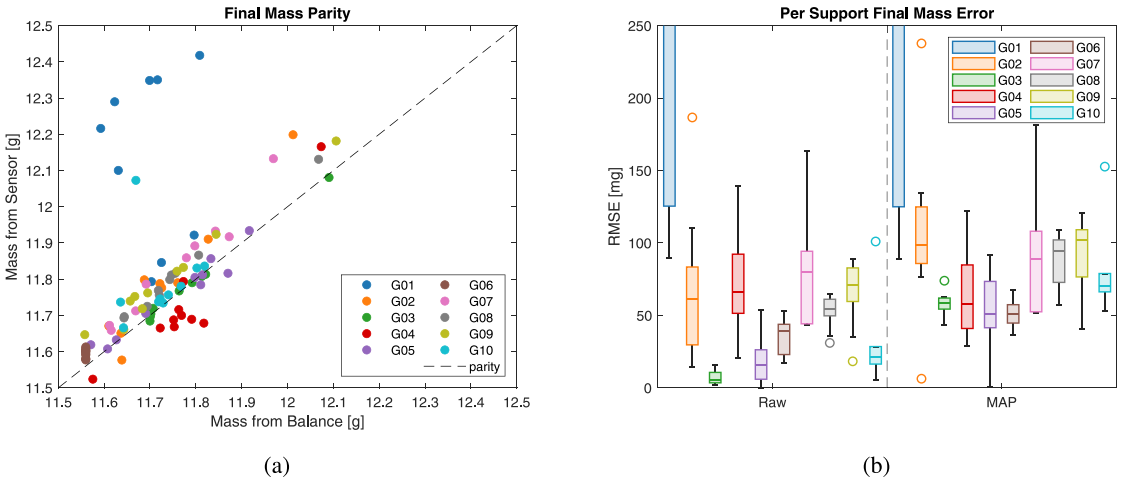

Fig. 19. Fig. 19(a) shows a parity plot for the final vial weight after sublimation as reported by the mass sensor without MAP and as measured on an analytical balance. Fig. 19(b) summarizes the error in the sensor measurements both without and with the MAP update. While the sensors generally perform consistently, G01 has a larger error because its vial basket contacts its sensor base before sublimation ends.

of 95 mg and a median value of 73 mg. Although this error exceeds the desired accuracy in Section 2, it is reasonable given the expected minimum in situ error discussed above. Fig. 19(b) shows that while the use of the MAP method reduces variation in the mass estimate error, it also biases the estimates away from their true value. This bias likely occurs because the vials begin to sublimate as soon as they enter the vacuum environment, so some mass change occurs before the initial AprilTag deviation for each sensor is measured.

8. Conclusion

This article presents the design and testing of a spring-wire based mechanical sensor that directly measures the mass of vials during lyophilization. The sensor carries a vial suspended from a pair of partial helical spring wires. The motion of AprilTags at the ends of sensing arms on the spring wires is tracked by a camera as water sublimates from the product in the vial, providing sublimation rates for individual vials. Ten of these sensors were manufactured for 10R vials with a 3 mL fill of solution, and they were evaluated both on a reference balance for their absolute accuracy and in a lyophilizer for their performance in situ.

Data from the reference balance showed that third-order polynomials are required to capture the variation from unmodeled nonlinear effects on the measured optical fiducial motion. While these models had a median RMSE of 13 mg, this value was improved to 6.5 mg by using the maximum a posteriori method to refine the parameters. These results required 4.5 hr of calibration per support to achieve, but a combination of the maximum a posteriori method and sparse calibration data collection could achieve a median RMSE of 15 mg with only 20 min of data collection.

After these sensors were calibrated, they were assembled into an array, and their performance was evaluated in a lyophilization environment. The sensors had limited accuracy in predicting the final mass of the lyophilized product, achieving a median RMSE of 50 mg, likely due to hysteresis introduced by motion of the sensor assembly between measurements. Despite this reduced absolute accuracy, per vial sublimation rates are measured accurately and used to infer drying endpoints.

With their current level of performance, these sensors could be used to evaluate the spatial heterogeneity of drying in existing batch systems or to enable drying endpoint detection in emerging continuous lyophilizers. The online accuracy of these sensors can likely be improved by eliminating sources of friction from the array assembly, improving the determination of the sensor coordinate system, and measuring the initial displacement before freezing begins.

The theoretical resolution limit of the sensor can likely be improved by increasing the compliance of the sensor. This increase could be achieved without changing the footprint of the sensor by decreasing the sensing wire diameter or increasing the sensing arm length. Decreasing the sensing wire diameter could require using a stronger material, such as titanium, to ensure that the wire remains in its elastic regime, but a material change could significantly increase the sensor cost. The sensing arm could be lengthened by replacing the physical sensing arm with an optical lever, such that the effective motion created by the slope change at the helical arm tip is amplified further without occupying additional space within the lyophilizer.

CRediT authorship contribution statement

Steven J. Burcat: Writing – original draft, Visualization, Methodology, Investigation. **Rohan P. Kadambi:** Writing – original draft, Visualization, Software, Methodology, Investigation, Formal analysis. **Lorenzo Stratta:** Methodology, Investigation, Conceptualization. **Richard D. Braatz:** Writing – review & editing, Supervision, Methodology, Funding acquisition, Conceptualization. **Roberto Pisano:** Writing – review & editing, Conceptualization. **Bernhardt L. Trout:** Writing – review & editing, Supervision, Methodology, Funding acquisition, Conceptualization. **Alexander H. Slocum:** Writing – review & editing, Supervision, Methodology, Funding acquisition, Conceptualization.

Declaration of competing interest

The authors declare that they have no known competing financial interests or personal relationships that could have appeared to influence the work reported in this paper.

Acknowledgments

This work was supported by the Food and Drug Administration, United States under Grant FD006755-02. The vacuum chamber used for the lyophilization experiments was manufactured by Josh Dittrich at StartSomething in Somerville, MA.

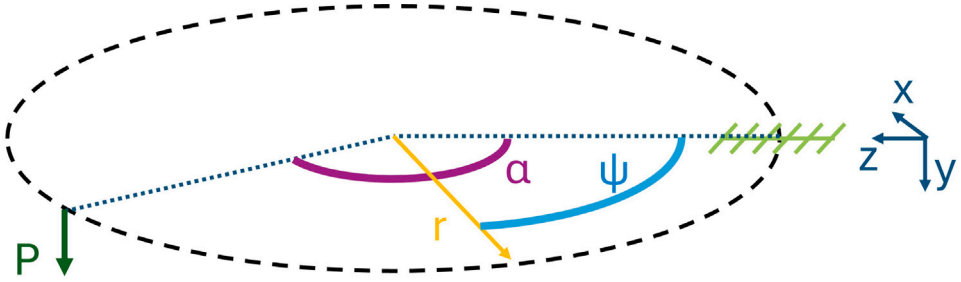

Fig. 20. A diagram showing a curved cantilevered beam loaded perpendicular to the curvature plane. P is the out of plane force, α is the total angle of the wire arc, and r is the radius of curvature of the wire arc.

Table 2
The z deflection calculation based on the theoretical deflection of a curved cantilever beam loaded perpendicularly to the plane of its curvature using the parameters used in this work. This calculation is based on 3 grams of mass change, representative of the 3 grams of water that is sublimated from a vial used during the development of the sensor in this work.

Parameter	Name	Value	Units	Formula
Wire arc radius	R_w	16	mm	
Number of wires	N_w	2		
Total vial mass	m_v	3	g	
Force per wire	P	0.01	N	$:= m_v \times (9.8/1000/N_w)$
Wire elastic modulus	E_w	194,000	N/mm	
Wire shear modulus	G_w	74,600	N/mm	
Wire diameter	D_w	0.014	in	
Wire bending moment of inertia	I_w	0.0008	mm^4	$:= \pi D_w/64$
Wire torsion moment of inertia	J_w	0.0016	mm^4	$:= \pi D_w/32$
Wire stiffness ratio	β	1.30		$:= (E_w I_w)/(G_w J_w)$
		0.3556	mm	
Wire arc	arc_w	140	degrees	
		2.4	rad	
Wire tip bending deflection	δ_B	0.58	mm	$:= 32PR_w^3/(PIE_w D_w^4) \times (arc_w - \sin(arc_w) \times \cos(arc_w))$
Wire tip torsion deflection	δ_T	1.10	mm	$:= 8PR_w^3/(PIG_w D_w^4) \times (6arc_w - 8\sin(arc_w) + \sin(2arc_w))$
Wire tip total deflection	δ_z	1.68	mm	$:= \delta_B + \delta_T$
Slope constant 1	C_1	−2.89		$:= ((1+\beta)/2) \times (arc_w\cos(arc_w) - \sin(arc_w))$
Slope constant 2	C_2	−0.49		$:= ((1+\beta)/2) \times arc_w\sin(arc_w) - \beta(1 - \cos(arc_w))$
Wire tip bending slope term	θ_B	0.047	rad	$:= (PR_w^2)/(E_w I_w) \times (C_2\cos(arc_w) - C_1\sin(arc_w))$
Wire tip torsion slope term	θ_T	0.055	rad	$:= (PR_w^2)/(E_w I_w) \times (C_1\cos(arc_w) + C_2\sin(arc_w))$
Sensing arm length	L_{arm}	50	mm	
Bending slope motion	δ_{s_B}	2.349	mm	$:= \theta_B L_{arm}$
Torsion slope motion	δ_{s_T}	2.761	mm	$:= \theta_T L_{arm}$
Total tip motion	δ_s	3.625	mm	$:= \left(\delta_{s_B}^2 + \delta_{s_T}^2\right)^{1/2}$

Table 3
Preload angle calculation based on the theoretical deflection of a curved cantilever beam loaded perpendicularly to the plane of its curvature using the parameters used in this work. This calculation is based on a 15 gram mass representative of the 9 gram 10R vial, the 2 gram vial cap, and the 4 gram vial basket used during the development of the sensor in this work.

Parameter	Name	Value	Units	Formula
Wire arc radius	R_w	16	mm	
Number of wires	N_w	2		
Total vial mass	m_v	15	g	
Force per wire	P	0.07	N	$:= m_v \times 9.8/1000/N_w$
Wire elastic modulus	E_w	194,000	N/mm	
Wire shear modulus	G_w	74,600	N/mm	
Wire diameter	D_w	0.014	in	
		0.3556	mm	
Wire arc	arc_w	140	degrees	
		2.4	rad	
Wire tip bending deflection	δ_B	2.90	mm	$:= (32PR_w^3/(PIE_w D_w^4)) \times (arc_w - \sin(arc_w) \times \cos(arc_w))$
Wire tip torsion deflection	δ_T	5.48	mm	$:= (8PR_w^3/(PIG_w D_w^4)) \times (6arc_w - 8\sin(arc_w) + \sin(2arc_w))$
Wire tip total deflection	δ_z	8.39	mm	$:= \delta_B + \delta_T$
Base to tip chord	$L_{preload}$	30.1	mm	$:= R_w(2(1 - \cos(arc_w)))^{1/2}$
Preload angle	θ_0	0.28	rad	$:= \text{asin}(\delta_z/L_{preload})$
		16.2	deg	

Appendix A. Mechanical concept: Additional considerations

A.1. Spring wire mechanics

The problem setup appears in Fig. 20.

Timoshenko shows that the strain energy for the curved beam can be found using the relationship

$$U = \int_0^x \left(\frac{M_x^2}{2EI_x} + \frac{M_z^2}{2GI_p}\right) r d\psi \tag{9}$$

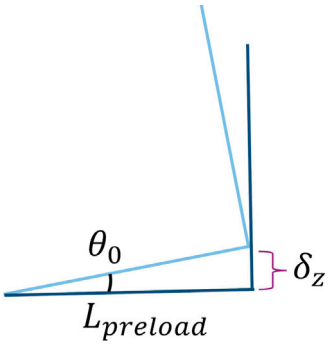

Fig. 21. The preload angle for the sensing wire is calculated based on the vertical deflection of the wire created by the empty vial, vial cap, and vial basket mass.

where M_x is the bending moment, E is the beam's Young's Modulus, I_x is the beam's second moment of inertia, M_z is the torsional moment, G is the beam's torsional rigidity, and I_p is the beam's polar moment of inertia. These moment loads are functions of the distance between the root and the end of the beam, and they can be expressed by the relationships

$$M_x = -Pr\sin(\alpha-\psi), \qquad M_z = Pr[1-\cos(\alpha-\psi)]. \tag{10}$$

The strain energy can be separated into its bending (U_x) and torsional (U_z) components,

$$U_x = \int_0^\alpha \frac{M_x^2 r}{2EI_x}d\psi, U_z = \int_0^\alpha \frac{M_z^2 r}{2GI_p}d\psi. \tag{11}$$

Taking the partial derivative of strain energy with respect to the load P results in

$$\delta = \frac{\partial U}{\partial P} = \frac{Pr^3}{EI_x}\int_0^\alpha \sin^2(\alpha-\psi) + \frac{EI_x}{GI_p}[1-\cos(\alpha-\psi)]^2 d\psi. \tag{12}$$

The explicit bending and torsional deflections can be split up as before, as seen in

$$\begin{aligned}\delta_x &= \frac{\partial U_x}{\partial P} = \frac{Pr^3}{EI_x}\int_0^\alpha \sin^2(\alpha-\psi)d\psi,\\ \delta_z &= \frac{\partial U_z}{\partial P} = \frac{Pr^3}{GI_p}\int_0^\alpha [1-\cos(\alpha-\psi)]^2 d\psi.\end{aligned} \tag{13}$$

Using the choice of a circular wire geometry, the moments of inertia can be substituted in to get the final deflection relationships shown in Eq. (1):

$$\delta_x = \frac{32Pr^3}{\pi Ed^4}(\alpha-\sin(\alpha)\cos(\alpha)), \qquad \delta_z = \frac{8Pr^3}{\pi Gd^4}(6\alpha-8\sin(\alpha)+\sin(2\alpha)). \tag{14}$$

Because the slope is affected by the bending and torsion loads in different directions, their net effects are evaluated based on a tabulated result from Roark's Formulas for Stress and Strain [20]. The slope contributions,

$$\theta_{\text{torsion}} = \frac{mgr^2}{EI}(C_1\cos(\alpha)+C_2\sin(\alpha)), \quad \theta_{\text{bending}} = \frac{mgr^2}{EI}(C_2\cos(\alpha)-C_1\sin(\alpha)), \tag{15}$$

and their relevant constants,

$$C_1 = \frac{1+\beta}{2}[\alpha\cos(\alpha)-\sin(\alpha)], \; C_2 = \frac{1+\beta}{2}[\alpha\sin(\alpha)-\beta[1-\cos(\alpha)]], \tag{16}$$

are copied here using variables consistent with this paper and evaluated at the end of the curved beam. The value of $\beta = \frac{EI}{GK}$ is 1.3 for a solid circular cross section wire with a Poisson ratio of approximately 0.3.

A.2. Example evaluation of the model

This appendix contains example calculations using the design spreadsheet for the expected vertical displacement, horizontal displacement and required preload angle for the sensing wires. This spreadsheet assumes a system layout including two wire beams each with the same circular curve and loaded equally at their free ends. First, Table 2 evaluates the model described in Section 3 for the final wire geometry. This table can be recreated using the provided design spreadsheet.

Second, Table 3 shows the calculation required for the preload angle. This angle is calculated based on the expected vertical deflection of the wire from the unloaded to dry vial state as shown in Fig. 21.

Appendix B. AprilTag data processing

This script provides the basic outline for how the `readAprilTag()` function can be used to convert data collected from the hardware described in Section 5.1. First, several constants are declared for which AprilTags are tracked and which video files should be analyzed.

```
% AprilTag family of tags
tag_family = "tag36h11";
% IDs of AprilTags to track
ids_track = [1 2];
% Dummy Video numbers
vid_index = 1:19;
% Physical Edge Length of the Tags
edge_size_mm = 3;
% Canon T7i auto-naming for video files follows: "MVI_####.MOV"
vid_file_list = arrayfun(@(x) sprintf("MVI_%04d.MOV", x), 1:19);
```

Next array variables are declared to store the location of the centroid of each tag as well as the average edge length of both tag across each video.

```
% Pre allocate arrays for the observables
t1_centroid_vid_list = zeros(numel(vid_file_list), 2);
t2_centroid_vid_list = zeros(numel(vid_file_list), 2);
edge_list_vid_px = zeros(size(vid_file_list));
```

Then, the code iterates over each video file and each frame of each video file calling `readAprilTag()` on each frame.

```
% Iterate over videos
for i = 1:numel(vid_file_list)
    v = VideoReader(vid_file_list(i));
    edge_list_frame = zeros(v.NumFrames, 2);
    t1_centroid_frame_list = zeros(v.NumFrames, 2);
    t2_centroid_frame_list = zeros(v.NumFrames, 2);
    % Iterate over each frame
    for j = 1:v.NumFrames
        [ids, locs] = readAprilTag(v.read(j), tag_family);
        % Extract the corners of the tags we plan to track
        locs_1 = squeeze(locs(:,:, ids == ids_track(1)));
        locs_2 = squeeze(locs(:,:, ids == ids_track(2)));
        % Calculate the centroids
        t1_centroid_frame_list(j,:) = mean(locs_1,1);
        t2_centroid_frame_list(j,:) = mean(locs_2,1);
        % Calculate the average edge Lengths
        % stack the first row on the bottom to get the last edge
```

```
        locs_1 = [locs_1; locs_1(1,:)];
        locs_2 = [locs_2; locs_2(1,:)];
        edge_list_frame(j,1) = mean(vecnorm(diff(
            locs_1(:,:))), 2,2);
        edge_list_frame(j,2) = mean(vecnorm(diff(
            locs_2(:,:))), 2,2);
    end
    % Store the average positions
    t1_centroid_vid_list = mean(t1_centroid_frame_list
        ,1);
    t2_centroid_vid_list = mean(t2_centroid_frame_list
        ,1);
    edge_list_vid_px(i) = mean(edge_list_frame, "all")
        ;
end
```

Finally, the deviations from the position recorded at the lightest mass (the first video) and the remaining videos is recorded and the mean deviation for both tags can be computed. This final, per video average deviation is then rescaled using the per video edge length and the known dimension of the AprilTag to compute a final deviation in physical units.

```
% Compute the deviations
dev_t1 = vecnorm(t1_centroid_vid_list -
    t1_centroid_vid_list(1,:),2,2);
dev_t2 = vecnorm(t1_centroid_vid_list -
    t1_centroid_vid_list(1,:),2,2);
dev_bar_px = mean([dev_t1 dev_t2], 2);

% Scale to physical units
dev_bar_mm = dev_bar_px./edge_list_vid_px.*
    edge_size_mm;
```

This code can also be modified to detect a set of reference AprilTags, `ids_ref`, in the innermost loop. This modification enables the per-frame coordinate-system correction required by Section 5.2.1.

Appendix C. Variations in component masses

The empirical variation in component masses was measured explicitly to understand what range of masses the mass sensing system must be tolerant to (see Fig. 22).

Appendix D. Sensitivity of the MAP procedure to σ_E

Fig. 23 shows that sensitivity of the final RMSE for the offline fitting data to the choice of σ_E. The precise value chosen for σ_E is not important as long as it is sufficiently small. Specifically, the results are insensitive to the value of σ_E once it is less than the underlying noise (from the replicate variation, 16 mg, see Section 7.1.1).

Appendix E. Comparison of noise sources

There is an increase in the noise floor between the offline calibration and the online setup with the motion system disabled that can likely be attributed to the reduction in zoom required to fit two full sensors in the camera frame for online testing. However, when the sensors are repeatedly measured (at a constant mass) between motions of the sensor array, the noise level shown in Fig. 24 increases dramatically.

Appendix F. Description of supplementary material

SM01_CurvWireSens.xlsx: A design spreadsheet used to determine the key parameters for a spring wire mass sensor based on geometry constraints and desired sensor resolution.

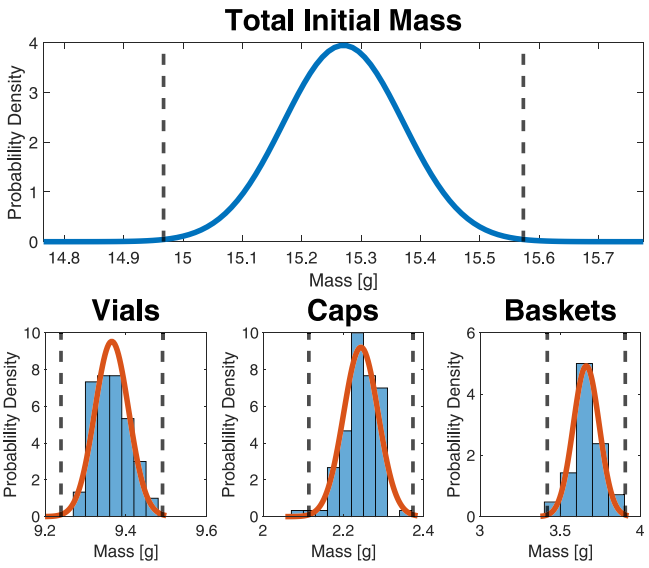

Fig. 22. Distributions collected by measuring 100 vials, 100 caps, and 42 baskets. After fitting each to a normal distribution the 3σ cutoffs for the total mass distribution was used to extend the desired fitting range.

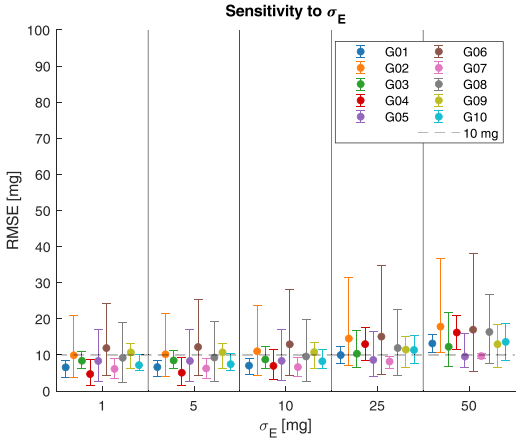

Fig. 23. The root-mean-squared error for $\sigma_E = 1, 5, 10, 25, 50$ for a third-order model generated using the procedure described in Section 6.2.2.

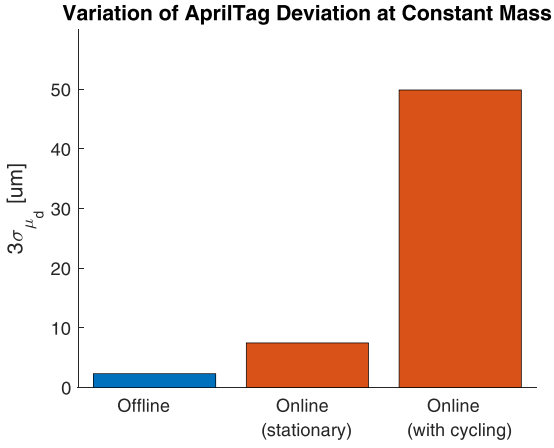

Fig. 24. Comparison of the 3σ noise floor for AprilTag deviation calculations at a constant mass across the online and offline setups.

SM02_offline_vial_motion_top.gif: An animated gif showing the motion of the AprilTags as the mass in the sensor changes.

SM03_online_vial_motion_side.mp4: A video showing the vertical motion of the vial in the sensor as water sublimates out of the vial.

SM04_TBD_cache_file.mat: A MATLAB cache file containing the measured AprilTag position, mass, and pressure data collected and used to generate the plots in this work.

SM05_TBD_example_loading.m: Example code for how to load and interact with the data in SM04_TBD_cache_file.mat.

Supplementary material related to this article can be found online at https://doi.org/10.1016/j.precisioneng.2025.07.007.

Data availability

A MATLAB cache file is included in the supplementary material which contains tables of AprilTag positions and corresponding supported masses of the sensor for both the offline calibration and online testing datasets.

References

[1] Rey L, May JC. Freeze-drying/lyophilization of pharmaceutical and biological products. 3rd ed. 2016.

[2] Horn J, Friess W. Detection of collapse and crystallization of saccharide, protein, and mannitol formulations by optical fibers in lyophilization. Front Chem 2018;6(JAN):327729.

[3] Johnson RE, Kirchhoff CF, Gaud HT. Mannitol–sucrose mixtures—Versatile formulations for protein lyophilization. J Pharm Sci 2002;91(4):914–22.

[4] Capozzi LC, Trout BL, Pisano R. From batch to continuous: Freeze-drying of suspended vials for pharmaceuticals in unit-doses. Ind Eng Chem Res 2019;58(4):1635–49.

[5] Leys L, Vanbillemont B, Van Bockstal PJ, Lammens J, Nuytten G, Corver J, et al. A primary drying model-based comparison of conventional batch freeze-drying to continuous spin-freeze-drying for unit doses. Eur J Pharmaceut Biopharmaceut 2020;157:97–107.

[6] Rambhatla S, Tchessalov S, Pikal MJ. Heat and mass transfer scale-up issues during freeze-drying, III: Control and characterization of dryer differences via operational qualification tests. AAPS PharmSciTech 2006;7(2):E61–70.

[7] Fissore D, Pisano R, Barresi AA. On the methods based on the pressure rise test for monitoring a freeze-drying process. Dry Technol 2010;29(1):73–90.

[8] Patel SM, Doen T, Pikal MJ. Determination of end point of primary drying in freeze-drying process control. AAPS PharmSciTech 2010;11(1):73–84.

[9] Pisano R. Automatic control of a freeze-drying process: Detection of the end point of primary drying. Dry Technol 2022;40(1).

[10] Kessler WJ, Gong E. Tunable diode laser absorption spectroscopy in lyophilization. Methods Pharmacol Toxicol 2019;113–41.

[11] Pisano R, Fissore D, Barresi AA. In-line and off-line optimization of freeze-drying cycles for pharmaceutical products. Dry Technol 2013;31(8):905–19.

[12] Tchessalov S, Shalaev E, Bhatnagar B, Nail S, Alexeenko A, Jameel F, et al. Best practices and guidelines (2022) for scale-up and tech transfer in freeze-drying based on case studies. Part 1: Challenges during scale up and transfer. AAPS PharmSciTech 2023;24(1):1–21.

[13] Rovero G, Ghio S, Barresi AA. Development of a prototype capacitive balance for freeze-drying studies. Chem Eng Sci 2001;56(11):3575–84.

[14] Barresi AA, Pisano R, Fissore D, Rasetto V, Velardi SA, Vallan A, et al. Monitoring of the primary drying of a lyophilization process in vials. Chem Eng Process: Process Intensif 2009;48(1):408–23.

[15] Roth C, Winter G, Lee G. Continuous measurement of drying rate of crystalline and amorphous systems during freeze-drying using an in situ microbalance technique. J Pharm Sci 2001;90(9):1345–55.

[16] Awotwe-Otoo D, Khan MA. Lyophilization of biologics: An FDA perspective. Lyophilized Biol Vaccines 2015;341–59.

[17] Rosas JG, de Waard H, De Beer T, Vervaet C, Remon JP, Hinrichs WL, et al. NIR spectroscopy for the in-line monitoring of a multicomponent formulation during the entire freeze-drying process. J Pharm Biomed Anal 2014;97:39–46.

[18] Pisano R, Arsiccio A, Capozzi LC, Trout BL. Achieving continuous manufacturing in lyophilization: Technologies and approaches. Eur J Pharmaceut Biopharmaceut 2019;142:265–79.

[19] Timoshenko S. Strength of materials part I: Elemental theory and problems. Huntington: Robert E. Krieger Publishing Co., Inc; 1958, p. 410–2.

[20] Roark RJ, Young WC, Plunkett R. Formulas for stress and strain. J Appl Mech 1976;43(3).

[21] O'Connell E. method for continuous inspection of product weight during lyophilization [Master's thesis], Cambridge: Massachusetts Institute of Technology; 2021.

[22] Wang J, Olson E. AprilTag 2: Efficient and robust fiducial detection. IEEE Int Conf Intell Robot Syst 2016;2016-November:4193–8.

[23] James G, Witten D, Hastie T, Tibshirani R. An introduction to statistical learning: with applications in R. 2nd ed. New York: Springer; 2021.

[24] Beck JV, Arnold KJ. Parameter estimation in engineering and science. New York: John Wiley & Sons; 1977.